JOURNAL OF PROPULSION AND POWER
Vol. 11, No. 2, March–April 1995

Numerical Investigation of Bluff-Body Stabilized Microwave Plasmas

S. Venkateswaran* and C. L. Merkle†
Pennsylvania State University, University Park, Pennsylvania 16802

Microwave heating of gases for space propulsion applications is addressed analytically by means of coupled solutions of the Navier–Stokes and Maxwell equations. The model is validated using experimental measurements of bluff-body stabilized microwave plasmas sustained in a resonant cavity. The size, shape, and location of the plasma are reasonably well-predicted, as are its overall thermal efficiency, coupling efficiency, and peak temperature. Parametric trends such as the effect of power and mass flow variations on thruster performance verify that the model incorporates the dominant physical processes of the plasma-fluid-dynamic interaction. In addition, the predictions indicate that the size of the plasma strongly influences the plasma temperature and its absorption characteristics. Proper design of the flow tube/bluff-body configuration enables the control of the plasma size and, hence, the plasma characteristics. This enables high-coupling efficiencies to be obtained at high power levels and, along with control of the mass flow to minimize wall heat, high thruster performance may be realized. Preliminary efforts to maximize performance resulted in specific impulse predictions of 600 s. Additional work is needed to identify methods for increasing the peak powers and to study size scale-up issues.

Introduction

MICROWAVE heating of gases is one of several advanced concepts being considered for space propulsion applications.[1] In general, those concepts that employ electromagnetic radiation (such as lasers, solar energy, thermal arcjets, or microwaves) as the energy source in an otherwise conventional rocket engine are collectively referred to as electrothermal thruster concepts.[2] Electrothermal thrusters possess two main advantages over conventional chemical propulsion systems: 1) the working fluid may be chosen based on its molecular weight rather than its chemical potential (hydrogen or helium are normally used), and 2) the gas may be heated to much higher temperatures. Both the low molecular weight and the high gas temperatures result in higher nozzle exit velocities leading to increased specific impulses *Isp*, compared to chemical systems. The thrust levels of these devices range from low to moderate (1–1000 N), which make them suitable for orbital transfer vehicles and satellite maneuvering, but not for high thrust applications such as liftoff.

In the area of laser and arcjet propulsion, considerable research—both experimental and theoretical—has been accomplished over the last decade, demonstrating the potential feasibility of these concepts. On the other hand, microwave propulsion is a relatively new entrant to the field, although the generation of microwave discharges in gases has been studied in the USSR[3,4] and Japan[5] since the 1970s. In the last few years, several experimental programs in the U.S.[6–10] have started studying the application of microwave plasmas for space propulsion. The microwave propulsion concept has several advantages over other electrothermal concepts; in particular, gas absorptivities are very high at microwave frequencies and microwave generation is very efficient. At the present time, experiments are targeted toward understanding the basic physics of microwave discharges and evaluating the potential performance of the propulsion system.

Theoretical analysis of the microwave heating of gases has hitherto received limited attention. The present authors recently reported the first results of a two-dimensional model of free-floating microwave plasmas sustained in a resonant cavity.[11] In a resonant cavity configuration, the microwaves are introduced into a cylindrical cavity that is tuned so that the microwaves form a standing wave pattern in the cavity. The gas flows in a quartz tube that is enclosed by the microwave cavity and gas breakdown is induced at a point of maximum electric field intensity resulting in a steady plasma discharge. The analysis in Ref. 11 was coordinated with companion experiments using helium gas in a similar geometrical configuration.[9]

The aformentioned experiments with free-floating plasmas were limited to powers of about 500 W, because at higher powers the plasma tended to arc to the walls of the quartz tube. This tendency was attributed to the asymmetric location of the coupling probe that was used to introduce the microwaves into the resonant cavity. (In contrast, the computations employed an axisymmetric inlet for the microwaves and the problem was not encountered). Recent experiments have adopted a bluff-body stabilization device[10] in order to prevent the migration of the plasma toward the walls at higher powers. In this article we describe the adaptation of the previous analysis to study bluff-body stabilized plasmas. The validation of the model is accomplished by comparison with the experimental results reported in Ref. 12.

We begin by giving a brief description of the geometrical configuration used in the experiments,[10] followed by a description of the computational model used in the analysis. Then, we present computational results for representative plasma solutions. Results of various parametric studies such as the effect of varying the incident power, discharge pressure, and gas velocity are given. Comparison with experimental observations of plasma size and shape, coupling, and overall efficiency and plasma temperature are made to verify the accuracy of the computational predictions. Stability of the plasma under different conditions is discussed. Finally, estimates of thruster performance are made based on the predicted plasma-flow interactions. Based on these estimates, ways of ensuring the effective utilization of microwave energy are identified.

Received Sept. 16, 1991; revision received May 30, 1994; accepted for publication June 6, 1994.

*Research Associate, Propulsion Engineering Research Center, Department of Mechanical Engineering. Member AIAA.

†Professor, Propulsion Engineering Research Center, Department of Mechanical Engineering. Member AIAA.

Physical Model

Flowfield Configuration

The experimental setup given in Ref. 10 is used as the base geometry in the present analysis. This configuration is shown in Fig. 1 along with a typical body-fitted fluid-dynamic grid (101 × 61). A separate rectangular grid is used for the electromagnetic field (121 × 121, not shown). Helium gas flows from top to bottom in the hemispherical quartz tube that is fitted with an orifice plate at the lower end.

In the experiments, the microwaves are introduced into the surrounding cylindrical cavity by means of a coupling probe (shown by dashed lines). In the computations, to preserve axisymmetry, a coaxial waveguide supplying microwaves to the cavity is positioned on the bottom face of the cavity. A sliding short is used to tune the length of the cavity for a particular standing wave mode (Fig. 1 shows the undistorted TM_{011} mode that was used in all of the experiments). In the calculations as well as the experiments, the length of the cavity and the locations of the bluff body and the microwave inlet were adjusted to obtain maximum coupling. The TM_{011} mode has points of maximum field intensity at the two ends of the centerline axis of the cavity. In the experiments, the plasma was sustained at the upper node and the bluff body (diameter of 2 cm), which serves as a plasma-stabilization device, is positioned near this node. In addition to the experimental configuration, additional calculations were performed with a straight duct 10 cm in diam, and a bluff body 4.5 cm in diam to assess parametric effects.

Fluid-Dynamic Equations

The flow of gaseous helium is governed by the compressible Navier-Stokes equations along with appropriate terms for the interaction with the electromagnetic (EM) radiation. Because of the low Mach numbers encountered in the flow, we use the low-Mach-number formulation described by Choi and Merkle.[13] The low-Mach-number version of the equations possesses well-conditioned eigenvalues at arbitrarily low Mach numbers, and thus ensures robust convergence of the time-marching algorithm. For purposes of the numerical algorithm, the equations are written in the coupled vector form including the unsteady terms:

$$P\frac{\partial \boldsymbol{Q}}{\partial t}+\frac{\partial \boldsymbol{E}}{\partial x}+\frac{\partial \boldsymbol{F}}{\partial y}=\frac{\partial \boldsymbol{E}_v}{\partial x}+\frac{\partial \boldsymbol{F}_v}{\partial y}+\boldsymbol{H}_1+\boldsymbol{H}_2 \qquad (1)$$

where

$$P=\begin{bmatrix}1 & 0 & 0 & 0\\ u & \rho & 0 & 0\\ v & 0 & \rho & 0\\ T & 0 & 0 & \rho\end{bmatrix},\qquad \boldsymbol{Q}=\begin{bmatrix}p_1 y/\beta\\ uy\\ vy\\ Ty\end{bmatrix}$$

$$\boldsymbol{E}=\begin{bmatrix}\rho uy\\ (\rho u^2+\varepsilon p_1)y\\ \rho uvy\\ \rho uTy\end{bmatrix},\qquad \boldsymbol{F}=\begin{bmatrix}\rho vy\\ \rho uvy\\ (\rho v^2+\varepsilon p_1)y\\ \rho vTy\end{bmatrix}$$

$$\boldsymbol{E}_v=\begin{bmatrix}0\\ \frac{4}{3}\mu y\frac{\partial u}{\partial x}-\frac{2}{3}\mu y\frac{\partial v}{\partial y}\\ \mu y\frac{\partial v}{\partial x}+\mu y\frac{\partial u}{\partial y}\\ K_c y\frac{\partial T}{\partial x}\end{bmatrix}$$

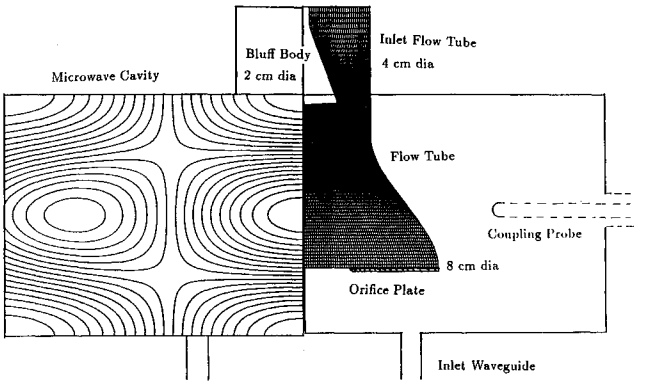

Fig. 1 Schematic of the base geometry used in the calculations. The hemispherical tube is shown with a typical fluid-dynamic grid. The TM_{011} mode in the microwave cavity is shown on the left side.

$$\boldsymbol{F}_v=\begin{bmatrix}0\\ \mu y\frac{\partial v}{\partial x}+\mu y\frac{\partial u}{\partial y}\\ -\frac{2}{3}\mu y\frac{\partial u}{\partial x}+\frac{4}{3}\mu y\frac{\partial v}{\partial y}\\ K_c y\frac{\partial T}{\partial y}\end{bmatrix}$$

$$\boldsymbol{H}_1=\begin{bmatrix}0\\ -\frac{2}{3}\frac{\partial}{\partial x}(\mu v)\\ \varepsilon p_1-\frac{4}{3}\frac{\mu v}{y}+\frac{2}{3}\mu\frac{\partial u}{\partial x}-\frac{2}{3}v\frac{\partial \mu}{\partial y}\end{bmatrix}$$

$$\boldsymbol{H}_2=\begin{bmatrix}0\\ -\rho g y-\mu' \bar{J}_y \bar{H}_\theta+\mu' \bar{J}_x \bar{H}_\theta\\ J\cdot Ey\end{bmatrix}$$

Here, ρ, u, v, p, and T represent the density, the x and y velocity components, and the pressure and temperature, respectively, while e is the total energy per unit volume and is given by $e=\rho C_v T+\frac{1}{2}\rho(u^2+v^2)$. The source terms are written as two vectors $\boldsymbol{H}_1$ and $\boldsymbol{H}_2$. The vector $\boldsymbol{H}_1$ contains the standard fluid-dynamic source terms that arise because of the axisymmetric coordinates. The vector $\boldsymbol{H}_2$ contains the source terms that arise from interactions with the electromagnetic radiation. These interaction terms are composed of the rms values of the electric E and magnetic H fields, and the electric current density J. The energy equation contains the heat source from electromagnetic radiation given by $J\cdot E$. In the momentum equations, the source terms arising from buoyancy and the Lorentz forces $J\times B$ are included. Radiation losses from the plasma were neglected in most of the calculations because they do not affect the overall energy balance significantly (as will be evident from the results discussed later).

In the computational model, the equations of motion are transformed to a generalized coordinate frame. The numerical solution of Eq. (1) is obtained by using Euler-implicit discretization in time along with central differences in space for both the inviscid and viscous fluxes. Douglas-Gunn approximate factorization is used for the efficient solution of the resulting matrix operator. The solution procedure involves a block-tridiagonal inversion for each coordinate direction at each time (or iteration) step. Further details on the algorithm are given in Ref. 11.

Maxwell Equations

The Maxwell equations for TM waves may be written in vector form analogous to the fluid-dynamic equations:

$$\frac{\partial \tilde{Q}}{\partial t} + \frac{\partial \tilde{E}}{\partial x} + \frac{\partial \tilde{F}}{\partial y} = \tilde{H} \tag{2}$$

$$\tilde{Q} = \begin{bmatrix} H_\theta y \\ E_y y \\ E_x y \\ J_y y \\ J_x y \end{bmatrix}, \quad \tilde{E} = \begin{bmatrix} (1/\mu')E_y y \\ (1/\varepsilon)H_\theta y \\ 0 \\ 0 \\ 0 \end{bmatrix}$$

$$\tilde{F} = \begin{bmatrix} -(1/\mu')E_x y \\ 0 \\ -(1/\varepsilon)H_\theta y \\ 0 \\ 0 \end{bmatrix}, \quad \tilde{H} = \begin{bmatrix} -(1/\mu')E_x \\ -(1/\varepsilon)J_y y \\ -(1/\varepsilon)J_x y \\ (\sigma_{dc}E_y - J_y)\nu_e y \\ (\sigma_{dc}E_x - J_x)\nu_e y \end{bmatrix}$$

In Eq. (2), the first three rows represent the standard Maxwell's curl relations relating the magnetic field H_θ to the electric field E_x and E_y. To close the curl relations, we need equations for the electric current density J_x and J_y. These equations [given by the last two rows of Eq. (2)] are obtained from momentum considerations for the conducting electrons in the plasma.[14] Here, $\sigma_{dc} = n_e q^2/m_e$ is the direct current electrical conductivity of the plasma, q is the electronic charge, m_e is the mass of an electron, n_e is the electron number density, and ν_e is the collision frequency of the electron with the heavy particles.

Local thermal equilibrium (LTE) is assumed between the electrons and heavy particles. Our results show that this assumption is reasonably accurate at atmospheric pressures, and very accurate at pressures of 3 atm or higher. Accordingly, the electron number density of the plasma is given by the Saha equation[15]; the electrical properties of the medium, σ_{dc} and ν_e, are calculated as given in Ref. 14; and the transport properties of helium are taken from Ref. 16.

The Maxwell equations are solved in the time domain by adopting an explicit time-marching procedure that is second-order accurate in time and space. The algorithm is similar to that conceived by Yee,[17] and is described in Ref. 11. The Maxwell solution yields an unsteady electromagnetic field. However, in terms of fluid time scales, the field is steady and is represented by the rms values of the time varying components. In the coupled solution procedure, for each Navier-Stokes time step, we calculate the EM field over several cycles (between 1–10), and then time-average to obtain the rms field. Typically, it is sufficient to compute a single EM cycle per iteration step.

Boundary Conditions

Inflow and outflow boundary conditions for both the fluid-dynamic and Maxwell equations are enforced by a vectorized implementation of the method of characteristics. For the fluid dynamics, the inlet temperature and gas velocity are specified at the inflow boundary along with an upstream-running characteristic. At the outflow boundary, the pressure is specified along with three outrunning characteristics. Symmetry and antisymmetry conditions are specified along the centerline while no-slip conditions, wall temperature, and the normal momentum equation are enforced on the walls.

The boundary conditions on the Maxwell equations for the EM field in the waveguide are particularly important. The tangential component of the electric field is specified to be zero on reflecting-wall boundaries. At the inlet section of the coaxial waveguide, the value of the electric field depends on the amount of power dissipated in the plasma and cannot be specified a priori. The correct quantities to keep fixed at these boundaries are the Riemann variable (or characteristic).[11] At the inlet section, the inward-running characteristic represents the incident power and is specified as a boundary condition, whereas the outgoing characteristic represents the reflected power component and is calculated from the solution.

Results and Discussion

Representative Plasma Solutions

Representative flowfield solutions for the plasma in the experimental hemispherical geometry are shown in Fig. 2. The discharge pressure is 1 atm, the incident-microwave power is 1 kW, and the inlet-gas velocity is 1.8 m/s. Under these inlet conditions, the Reynolds number is 8×10^1, while the mass flow rate is 0.11 g/s. Figure 2 shows the temperature and streamline contours. The temperature contours show the plasma located in the wake of the bluff body. The plasma appears to be oblong with its radial size being restricted by the size of the bluff body. The peak temperature in the core of the plasma is about 12,000 K.

The axial and electric field solutions (not shown) reveal that the plasma location coincides with the upper node of the TM_{011} mode in the microwave cavity. The field intensities are observed to be heavily distorted from their no-loss pattern near the plasma location, although away from the plasma, the overall TM_{011} mode shape is still retained. Whatever energy is not absorbed by the plasma is reflected back through the inlet waveguide. The coupling efficiency, defined as the percent of the incident power that is absorbed by the plasma, is 97% for this calculation. This means that 970 W of the incident power is absorbed by the plasma, while about 30 W is reflected back.

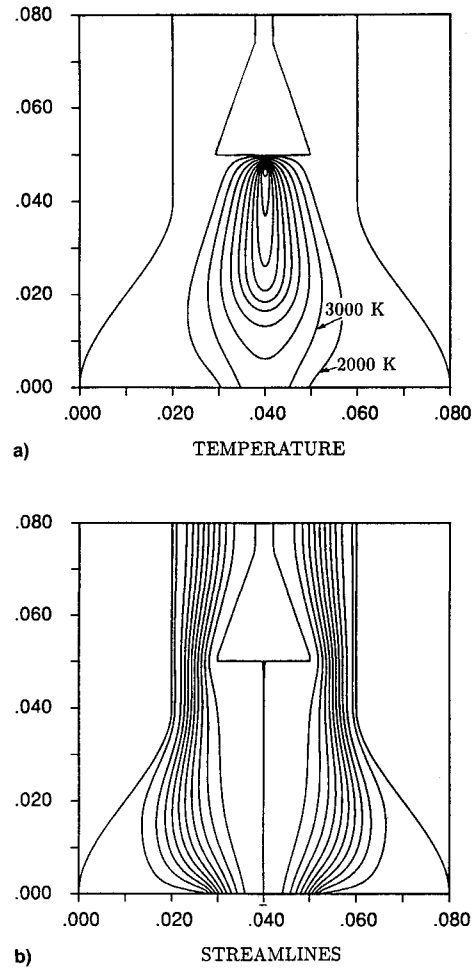

Fig. 2 Representative plasma solution for the hemispherical geometry showing a) temperature and b) streamline contours. P = 1 atm, power = 1 kW, $\dot{m}$ = 0.11 g/s, Re = 8×10^1.

The representative flowfield solution for an alternative geometrical configuration is shown in Fig. 3. Here, the flow tube is cylindrical (o.d. = 10 cm), and the bluff body diameter D_b is 4.5 cm, compared to 2 cm for the experimental geometry. Furthermore, the radius of the microwave cavity was reduced to 6 cm with a no-loss resonant length of 10 cm. (In comparison, the experimental setup has a cavity radius of 8.9 cm and a resonant length of 7.5 cm.) Figure 3 shows temperature and streamline contours for an incident power of 1 kW and a pressure of 1 atm. The corresponding mass flow rate is 1.1 g/s and the inlet Reynolds number is 3.25×10^2. The plasma is again seen to be sitting in the wake of the bluff body. The streamline contours now show evidence of recirculation because of the higher Reynolds number employed in this calculation.

Comparison of the plasmas in Figs. 2 and 3 (both of which are 1-kW plasmas) reveals several interesting features. The plasma in Fig. 3 is larger than the plasma in Fig. 2, both in radius and in length. Two factors contribute to the larger plasma size: 1) the larger bluff body size permits a larger radial plasma size, and 2) the longer length of the microwave cavity causes the plasma to be elongated. Furthermore, the peak plasma temperature in Fig. 4 is 9300 K, whereas that in Fig. 3 is 12,000 K. This difference in plasma temperatures is related to the difference in the plasma sizes, the smaller plasma being hotter than the larger plasma in order to maintain a sufficient degree of ionization within it. Note that the measurements and predictions of plasma temperature in free-floating plasmas[11] also yielded temperatures of about 9000–10,000 K, because the geometrical configuration in that case resulted in larger plasma sizes as well. In fact, most of the earlier experimental data on microwave plasmas[3–5] have indicated peak temperatures of about 10,000 K and, for this reason, the temperature measurements of 12,000 K for the current configuration[12] were originally considered questionable. The present calculations clearly show that the higher temperature is, indeed, justified. Furthermore, the calculations also show that it is possible to obtain control over the peak plasma temperature by adjusting the flow geometry and/or the microwave-cavity dimensions.

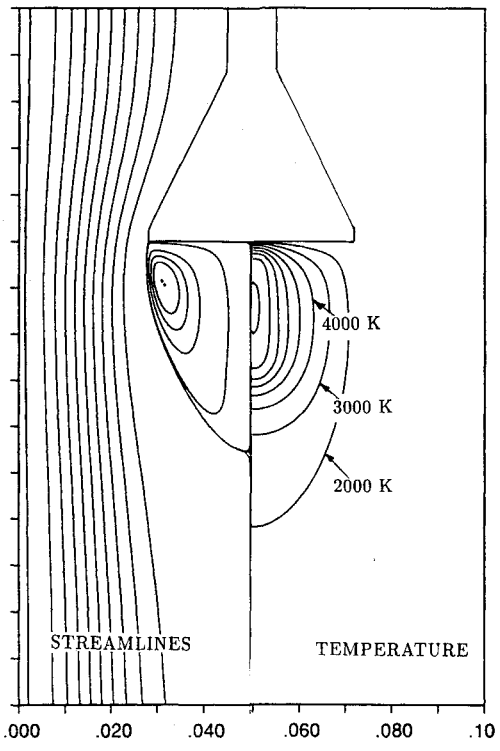

Fig. 3 Representative plasma solution for alternate configuration using a cylindrical flow tube and a larger bluff body (D_b = 4.5 cm). Streamlines are on the left and temperature contours are on the right. P = 1 atm, power = 1 kW, $\dot{m}$ = 1.1 g/s, Re = 3.25×10^2.

Effect of Increasing Incident Power

Figure 4 shows the computed plasma temperature contours for two different power levels, 750 W and 1.5 kW, at a discharge pressure of 2.5 atm. In general, the effect of increasing power is to increase the length of the plasma along with a slight radial growth as well (near the base of the plasma, this growth is restricted by the bluff body). Experimental photographs[12] of the plasmas under these conditions show similar qualitative trends. At 1.5 kW (Fig. 4b), both predictions and experiments show that the plasmas are long enough to reach the orifice plate; the experiments further show that the plasma bends toward the coupling probe and becomes slightly asymmetric at this power level. The computations are for an axisymmetric geometry and cannot show this effect.

Changing the incident power also causes changes in the coupling efficiency of the plasma. In Fig. 5, the coupling efficiency is plotted as a function of pressure for three different powers (1, 1.5, and 2 kW). Available experimental data (open markings) are also included for comparison to predictions (darkened markings). Estimated experimental uncertainty in coupling efficiency is about ±1% at these power levels. Both experiments and calculations predict very high coupling efficiencies (approaching 100%) at 1 kW. Increasing the power causes the coupling efficiency to drop. At higher powers, the geometric configuration (i.e., the sizes of the bluff body and the flow tube) restricts the maximum size of the plasma. Hence, the plasma starts to reflect a larger fraction of the incident power.

The computed coupling efficiency in Fig. 5 is observed to drop more rapidly at higher powers than that in the experiments; and at 2 kW, there is a discrepancy of about 5% in

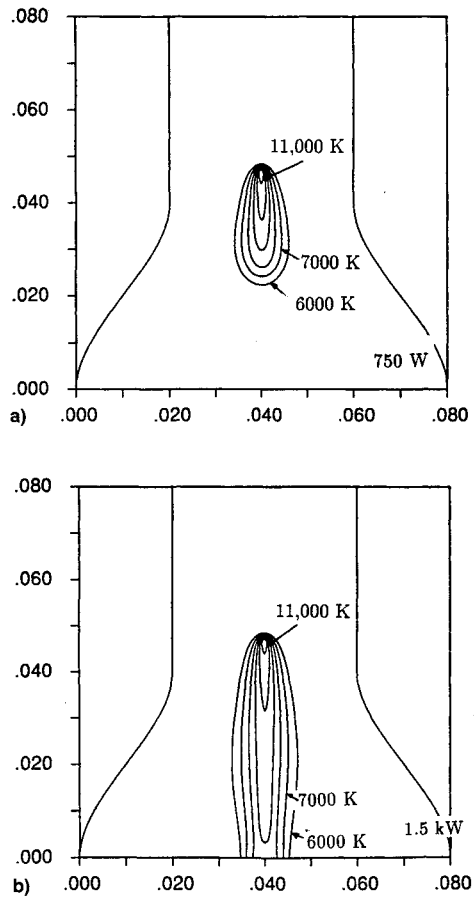

Fig. 4 Plasma temperature contours at two different power levels: a) 750 W and b) 1.5 kW. P = 2.5 atm.

Table 1 Coupling efficiency of the two different flow configurations

P, kW	1.0	2.0	3.0	4.0	6.0
A	98%	87%	68%	—	—
B	98%	98%	95%	85%	72%

Configuration A—hemispherical tube, D_b = 2 cm.
Configuration B—cylindrical tube, D_b = 4.5 cm.

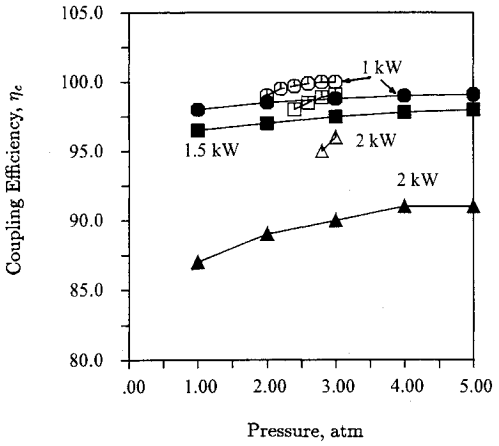

Fig. 5 Coupling efficiency vs pressure for different incident power levels. Experimental data are open symbols. Computational data are darkened symbols.

the results. In the experiments, the location of the coupling probe was continually adjusted (in the radial direction) for maximum coupling efficiency.[12] In contrast, in the computations, such a fine degree of tuning is difficult to perform since it would involve making several computations for each result. Thus, the location of the inlet waveguide was optimized for one representative case, and the remaining parametric studies were carried out with this same configuration. This is probably one reason why the computed coupling efficiencies are less than experimental values. A further reason is the asymmetry of the plasma at higher powers, which results in increased power absorption near the walls of the flow tube. The present axisymmetric computations cannot simulate this asymmetric behavior.

A more comprehensive survey of coupling efficiency with power level is summarized in Table 1 for both the hemispherical tube (A) and the cylindrical tube (B). The power levels here are chosen to be much higher than in the experiments to test the potential for going to higher net energies in the flow for propulsion applications. At low powers, both setups yield high efficiencies. At higher powers, however, the larger configuration promises better energy coupling. For a power of 3 kW, the larger configuration (B) gives a coupling efficiency of 95%, compared to 68% for the smaller setup (A). In fact, even at 6 kW, the coupling efficiency is still 72% for the larger tube. This is because the larger setup does not restrict the longitudinal growth of the plasma as much as the experimental setup does. However, it should be noted that, as the plasma grows larger, eventually its edge extends into a region where the electric field intensity is low and cannot support the plasma. Consequently, a decrease in the coupling efficiency is evident in Table 1 for configuration B as well.

Stability Boundary

When the power incident on the plasma is lowered below a certain threshold, the electric field cannot sustain a sufficient degree of ionization to maintain the discharge and, consequently, the plasma is extinguished. This threshold power, commonly referred to as the stability boundary, is shown in Fig. 6 as a function of the discharge pressure. The computational results are plotted for both the experimental hemisphere and the larger cylindrical tube. In both cases, the threshold power at 1-atm pressure is about 600–700 W. Increasing the pressure raises this threshold moderately. Experimental results for the bluff body TM_{011} plasma are limited to the three data points shown. At higher pressures, there seems to be fairly good agreement between the results. At low pressures, experiments with free-floating plasmas[9] have shown that plasmas may be stably sustained at powers down to about 200 W. Clearly, the computations overpredict the threshold at these low pressures. The most probable reason for this discrepancy is the assumption of local thermal equilibrium which is, of course, inapplicable in the limit of low pressures. In a later section, the comparison of computed plasma temperatures with measured electron temperatures also suggests that some amount of nonequilibrium may be present at pressures of 1–2 atm. Because our current interest is on microwave plasmas at high powers and pressures, extensions of the model to include nonequilibrium phenomena have not yet been implemented.

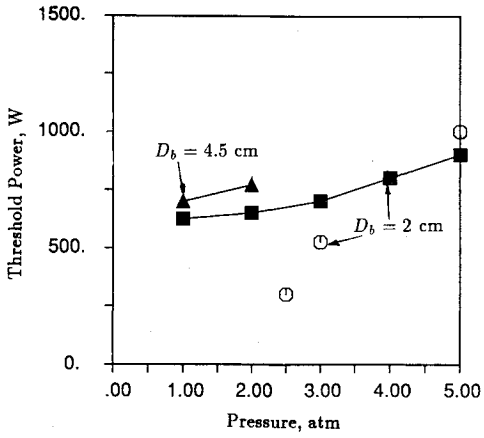

Fig. 6 Threshold power (or stability boundary) of the plasma as a function of discharge pressure. Experimental data are open symbols. Computational data are darkened symbols.

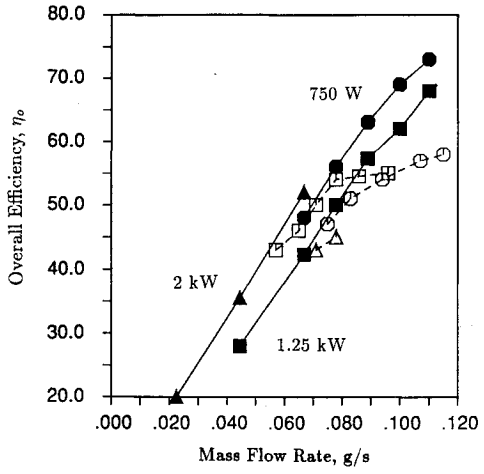

Fig. 7 Overall efficiency vs mass flow rate. Experimental data are open symbols. Computational data are darkened symbols.

Overall Efficiency

We have established that a high percentage of the incident power is absorbed by the plasma at powers up to 2 kW (for the hemispherical configuration). However, this does not mean that all this energy will be retained by the gas, and at least a part of this energy will be lost to the bluff body and the surrounding tube walls. The overall efficiency represents the ratio of the power retained by the gas after losses to the incident microwave power. Figure 7 shows the overall effi-

ciency plotted against the mass flow rate for three representative power levels, 750 W, 1.25, and 2 kW. Experimental observations are also included for comparison (estimated error ±12%).

The general behavior of the overall efficiency predictions with mass flow is in good agreement with experiments, although there are some differences. Both predictions and experiments indicate a fairly rapid increase in efficiency with increasing mass flow rate. This increase occurs because the faster flow velocities reduce the plasma spreading so that the hot gases are more closely confined to the center of the tube and less heat is lost through the walls. The level of the computed efficiencies is also quite well-predicted, showing that the predominant losses are properly accounted for. However, the experimental measurements show that the efficiency begins to level off at lower mass flow rates than do the predictions. The specific reasons for this are not known, but is probably due to high heat losses around the orifice region in the experiments. Finally, the predicted efficiencies at 2 kW are higher than the experimental values; but, as noted earlier, the experimental results at this higher power show considerable asymmetry, which undoubtedly increases the wall heating and reduces the thermal efficiencies.

Comparison of Peak Plasma Temperatures

The peak plasma temperatures predicted by the computations are compared to measurements of the electron temperature in Fig. 8. Under the approximation of local thermal equilibrium, the electron temperature and the gas temperature are equal. The comparison shows that the peak temperatures are fairly constant, ranging from 11,500 to 12,500 K for plasmas at pressures of 1–5 atm. The agreement between computations and experiments is very good at pressures above 3 atm. At lower pressures, the computations underpredict the temperatures by about 5–10%. While this is within the bounds of experimental error (about ±10%), the discrepancy may be an indication of some nonequilibrium behavior at these pressures.

Predictions for the peak temperature in the cylindrical flow tube with the larger bluff body are also given in Fig. 8. The predictions indicate a peak temperature of about 9000–10,000 K for this larger configuration—a result that is in sharp contrast with the results for the hemispherical tube, but in line with previous measurements of microwave plasma temperatures (as, e.g., the free-floating plasmas[9]). As mentioned earlier, this temperature difference is because the larger bluff-body diameter allows a larger plasma diameter, which increases the volume over which the energy is deposited and, consequently, lowers the peak temperature.

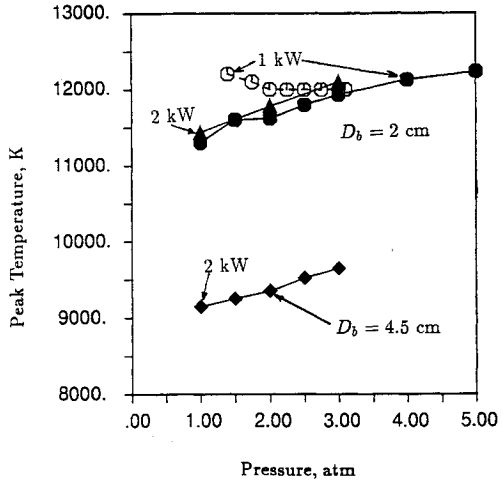

Fig. 8 Comparison of computed peak plasma temperatures (darkened symbols) with experimental data (open symbols).

Average Gas Temperature

The peak plasma temperature is an important characteristic of plasmas; however, the performance of the propulsion device depends not on the peak temperature, but on the average temperature to which the total mass of gas is heated. These two quantities can be very different because of the highly two-dimensional nature of the flowfield. Figure 9 shows the average gas temperature obtained at the exit of the hemispherical tube. Results are shown for four power levels as a function of the mass flow rate. At higher powers, more energy is added to the gas and the average gas temperature is higher. At 2 kW, the average temperature is 3000–3500 K, whereas at 750 W, it is only about 1000 K. The higher temperatures, at 1.5 and 2 kW, are a consequence of the fact that the plasma extends all the way up to the exit of the flow tube and heats a larger fraction of the gas flow. This result shows that it is crucial to employ relatively high powers to obtain high thruster performance.

In Fig. 9, for the 1.5- and 2-kW cases, the gas is seen to cool down with increasing mass flow rates. High mass flow rates result in effectively heating only a small portion of the flow. Figures 7 and 9, therefore, suggest that the efficient operation of the device imposes conflicting requirements—the mass flow rate should be high enough to reduce heat losses (maintaining high overall efficiencies) while, at the same time, it should be low enough to achieve high average gas temperatures. Thus, the design of a practical microwave thruster would involve a compromise between high performance and high thermal efficiency.

Thruster Performance

To get an estimate of the performance capability of the above system, the thrust and specific impulse of the thruster are computed assuming complete isentropic expansion of the gas at the exit of the hemispherical tube. These performance numbers are plotted on Figs. 10 and 11 against the mass flow rate for three power levels (750 W, 1.25 and 2 kW). Experimental evaluations[12] of these quantities are also included for comparison (error estimates are ±9% for *Isp* and ±3% for thrust). Both Figs. 10 and 11 show that the experimental data agree reasonably well with the predictions of thrust and specific impulse. From Fig. 10, we can see that the available *Isp* are about 350 s for the 750-W plasma, about 450 s for 1.25-kW plasma, and up to 600 s for the 2-kW plasma. These results are a direct consequence of the average gas temperatures presented in Fig. 9. Conventional chemical engines are capable of delivering *Isp* in the range of 300–500 s. The present microwave configuration therefore promises improved performance at high powers.

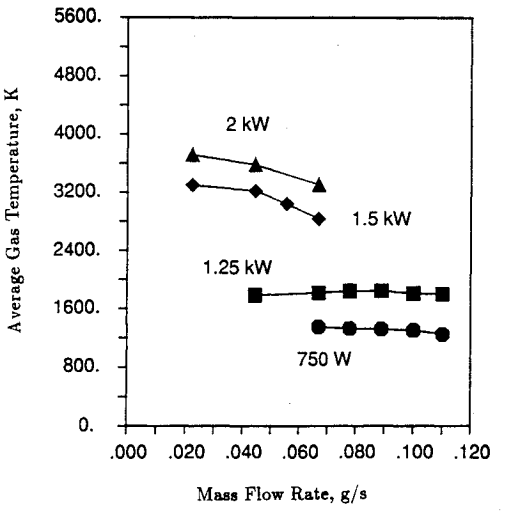

Fig. 9 Computed average gas temperatures vs mass flow rate at different incident power levels.

Table 2 Performance of microwave configuration B

P, kW	η_0, %	T_{av}, K	Isp, s	Th, N
2.0	57.5	1586	442	0.62
3.0	55.0	2295	520	0.73
4.0	48.0	2635	551	0.77
6.0	38.0	3150	600	0.84

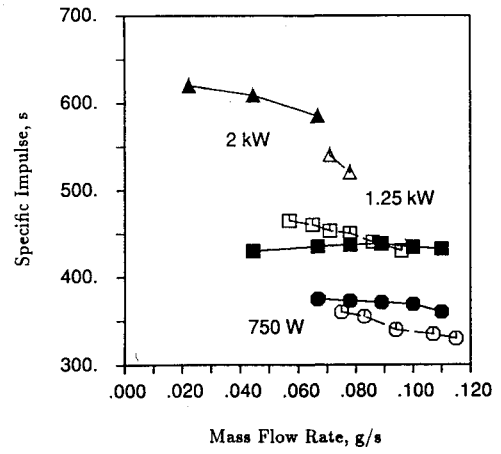

Fig. 10 Specific impulse vs mass flow rate. Experimental data are open symbols. Computational data are darkened symbols.

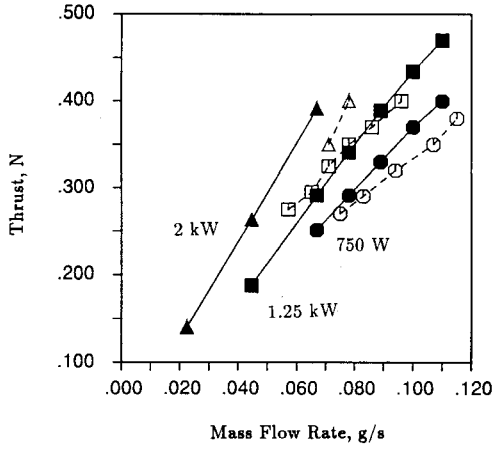

Fig. 11 Thrust vs mass flow rate. Experimental data are open symbols. Computational data are darkened symbols.

Thrust predictions are plotted on Fig. 11, which indicates thrust levels in the range of 0.1–0.5 N for the mass flow rates and powers used here. These extremely low thrusts are suitable for space propulsion such as stationkeeping and maneuvering. For achieving higher thrust levels, larger microwave powers will be required, and again, this represents an additional research challenge.

Similar performance estimates for the microwave plasmas sustained in the larger cylindrical flow tube are summarized in Table 2. In this case, because of the increased size of the tube, the mass flow rate at which optimum performance is obtained is considerably higher than the mass flows adopted for the experimental configuration. The mass flow rate employed in the calculations of Table 2 is 0.14 g/s. At low powers, the performance of the system is poor and the gas is heated to only about 1000 K; but at higher powers (6 kW), the average gas temperature is about 3000 K and the indicated Isp is about 600 s; a result that is qualitatively similar to that obtained for the experimental hemisphere. It is evident that more work needs to be done to identify flow configurations that would yield enhanced performance and theoretical analyses (such as the present one) would be invaluable in carrying out such exploratory studies.

Finally, we note that size scale-up in microwave thrusters is an important issue. While there is some room for geometric scaling, the size of the thruster is basically set by the wavelength of the microwaves. Changes in the microwave frequency from its present value of 2.45-GHz level represent one potential way for designing larger microwave engines.

Conclusions

Coupled solutions of the Navier-Stokes equations and the Maxwell equations are employed to analyze microwave plasmas in a resonant cavity and to identify the issues involved in the effective utilization of these plasmas for space propulsion. The analysis has been closely coordinated with companion experiments using a similar geometrical configuration. Additional calculations with a larger configuration have also been performed to study parametric effects at higher power levels.

The predicted results are compared to experimental measurements in order to verify model accuracy. Plasma size, shape, and location are well-predicted by the model; in particular, the bluff body serves as an excellent stabilization device and consistently maintains the plasma in its wake region. Coupling efficiencies up to 99% are predicted at low powers, a result that agrees well with measurements. At high powers (above 2 kW), the coupling efficiency drops because the geometrical configuration limits the growth of the plasma. Plasma peak temperatures are shown to be about 12,000 K, both by computations and experiments. The computations reveal that the peak temperature is a function of plasma size, a finding that explains previous temperature measurements (and calculations) of 10,000 K. Finally, the overall efficiency and the predicted thrust and specific impulse are in good overall agreement with experimental evaluations of these quantities.

The present analysis has provided a great deal of physical insight into the operation of a microwave plasma device. The major issue is that high average gas temperatures are required to obtain increased performance over conventional chemical propulsion systems. Calculations indicate average gas temperatures of about 3000 K at a power of 2 kW. Higher temperatures may be obtained if higher power levels are employed. However, at higher powers, the present configuration indicates low coupling efficiencies because the plasma size is limited by the geometry. Additional study is warranted to identify appropriate designs for high-power plasma devices. A related design issue is the optimization of the mass flow rate through the thruster to maximize the average gas temperature and, at the same time, to minimize the heat losses to the surroundings. It is evident that more work needs to be done to address these issues and theoretical analyses would be useful in complementing experimental work in these surveys.

Acknowledgment

This work was sponsored by the Air Force Office of Scientific Research, Bolling Air Force Base, Washington, DC, under Contract 89-0312.

References

[1]Micci, M. M., "Prospects of Microwave Heated Propulsion," AIAA Paper 84-1390, June 1984.

[2]Sovey, J. S., Hardy, T. L., and Englehart, M. A., "A Bibliography of Electrothermal Thruster Technology 1984," NASA TM 86998, 1986.

[3]Kapitza, P. L., "Free Plasma Filament in a High Frequency Field at High Pressure," *Soviet Physics—JETP*, Vol. 30, June 1970, pp. 973–1224.

[4]Meierovich, B. E., "Diffusion in a High Frequency Gas Discharge," *Soviet Physics—JETP*, Vol. 344, Feb. 1973, pp. 291–299.

[5]Arata, Y., Miyake, S., and Kobayashi, A., "High Power Micro-

wave Discharge in Atmospheric Hydrogen Gas Flow," *Journal of the Physical Society of Japan*, Vol. 44, March 1978, pp. 998–1003.

[6]Hawley, M. C., Asmussen, J., Filpus, J. W., Whitehair, S., Hoekstra, C., Morin, T. J., and Chapman, R., "Review of Research and Development on the Microwave Electrothermal Thruster," *Journal of Propulsion and Power*, Vol. 5, No. 6, 1989, pp. 703–712.

[7]Janson, S., Welle, R., Pollard, J., Crofton, M., Baumgartner, H., and Cohen, R., "The Physics of Chemistry of Radio Frequency and Microwave Thruster Plumes," AIAA Paper 91-1501, June 1991.

[8]Mueller, J., and Micci, M. M., "Microwave Electrothermal Thrusters Using Waveguide-Heated Plasmas," AIAA Paper 90-2562, July 1990.

[9]Balaam, P., and Micci, M. M., "Investigation of Free-Floating Nitrogen and Helium Plasmas Generated in a Microwave Resonant Cavity," AIAA Paper 89-2380, July 1989.

[10]Balaam, P., and Micci, M. M., "The Stabilization and Spectroscopic Study of Microwave Resonant Cavity Plasmas," AIAA Paper 90-2635, July 1990.

[11]Venkateswaran, S., Merkle, C. L., and Micci, M. M., "Analytical Modeling of Microwave Absorption in a Flowing Gas," AIAA Paper 90-1611, June 1990.

[12]Balaam, P., "Experimental Development of a Microwave Resonant Cavity Electrothermal Propulsion Device," Ph.D. Dissertation, Dept. of Aerospace Engineering, Pennsylvania State Univ., University Park, PA, Dec. 1990.

[13]Merkle, C. L., and Choi, Y.-H., "Computation of Low-Speed Flow with Heat Addition," *AIAA Journal*, Vol. 25, No. 6, 1987, pp. 831–838.

[14]Jahn, R., *Principles of Electric Propulsion*, McGraw–Hill, New York, 1968.

[15]Vicenti, W. G., and Kruger, C. H., *Introduction to Physical Gas Dynamics*, Kreiger Publishing Co., Malabar, FL, 1986.

[16]Lick, W. J., and Emmons, A. W., *Transport Properties of Helium from 200 to 12,000 K*, Harvard Univ. Press, Cambridge, MA, 1965.

[17]Yee, K. S., "Numerical Solution of Initial Boundary Value Problems Involving Maxwell's Equations in Isotropic Media," *IEEE Transactions on Antennas and Propagation*, AP-14, May 1966, pp. 302–307.